Journal of Materials Chemistry B

PAPER

View Article Online
View Journal



Cite this: DOI: 10.1039/d5tb02000j

# Control of site-specific deprotonation through mechanochemical interconversion of two ionic cocrystal forms of resveratrol

Bowyn D. Ziebarth, [a] Liulei Ma, [a] Gary C. George III [a] and Kristin M. Hutchins *[ab]

Received 5th September 2025,
Accepted 2nd March 2026

DOI: 10.1039/d5tb02000j

rsc.li/materials-b

In drug development, multicomponent pharmaceutical materials have become useful tools for improving the properties and efficacy of a drug. In addition to the active drug, inclusion of a second component in the solid can provide stabilization or increase solubility of the pharmaceutical. Resveratrol, an antioxidant with many potential pharmacological effects, is limited by low aqueous solubility. Cocrystallization with 4-aminopyridine, an FDA approved medication used in the treatment of multiple sclerosis, was utilized and two ionic cocrystal phases were obtained. The two phases differ by stoichiometry, water inclusion, and proton transfer site on resveratrol. Reversible interconversion between both phases was achieved mechanochemically, a rare occurrence among multicomponent solids. This system demonstrates the first ionic crystalline forms of resveratrol, significantly enhanced solubility, and a rare example of a cocrystal system exhibiting different deprotonation sites at molecular locations with identical functional groups. The presence of anionic resveratrol in the solid could enhance its antioxidant efficacy compared to neutral resveratrol or other antioxidants. Furthermore, resveratrol has been previously reported to improve clinical markers in a mice model of multiple sclerosis, indicating this combination could offer a unique dual-therapeutic treatment.



## 1. Introduction

Crystalline forms of pharmaceuticals are advantageous because they offer high purity, stability, and often straightforward quality control;[1,2] however, several factors, including hygroscopicity or polymorphism, can raise challenges in the development and marketing of crystalline-form drugs. Polymorphism refers to the ability of compounds to crystallize in more than one structural arrangement.[3] Control over polymorphism remains a critical aspect of drug development and materials science, requiring major investments of both time and money. This investment is necessary for pharmaceuticals because polymorphs often exhibit different properties, including solubility, stability, or tabletability, which necessitates extensive polymorph screening before marketing a drug.[4–7] Polymorphism is controlled primarily through tuning crystallization parameters such as solvent, temperature, time, or pressure.[7–10] Mechanochemistry, a method that uses physical impact to induce chemical changes, has also been used to control polymorphism.[11] For example, mechanochemical milling was recently applied to ritonavir, an antiviral medication that was recalled after isolation of form II prevented production of the more bioavailable form I. Specifically, extended milling of form II afforded form I when all prior experiments aimed at preparing form I or converting form II to form I were unsuccessful.[12] In other cases, conversion of one polymorph to another has been achieved through manipulation of temperature, pressure, solvent identity, solvent amount, crystallization method, and even the material used for milling vessels.[13] Methods that enable polymorphs to not only be converted from one to another, but be reversibly interconverted, would be especially useful in cases where one form exhibits superior properties, but is challenging to obtain, or when multiple forms show distinct and useful properties.[4]

In addition to pharmaceutical solids that contain only the drug molecule, pharmaceutical salts, cocrystals, and ionic cocrystals (*i.e.*, multicomponent solids) have also been developed to tune the physiochemical properties of drugs.[14] In such multicomponent solids, polymorphism is possible; however, additional types of polymorphism also arise including stoichiometric or solvatomorphic, which are polymorphs with variation in the stoichiometries of the molecular components or included solvents, respectively.[15] Although cocrystallization

[a] Department of Chemistry, University of Missouri, 601 S College Avenue, Columbia, Missouri, 65211, USA. E-mail: kristin.hutchins@missouri.edu
[b] MU Materials Science & Engineering Institute, University of Missouri, Columbia, Missouri, 65211, USA

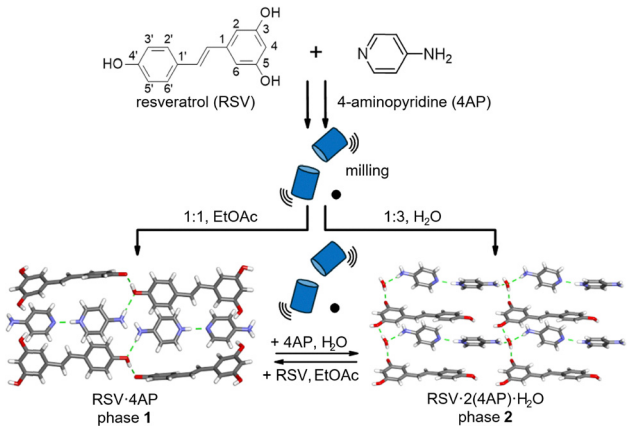


Scheme 1 Components of multicomponent solids (RSV and 4AP) highlighting mechanochemical synthesis of and interconversion between phase **1** and phase **2**.

using solution methods remains most common, mechanochemistry offers a way to screen for many different phases in a relatively rapid timeframe. Typically, two compounds are ground or milled together, with or without a small amount of solvent, then analyzed *via* powder X-ray diffraction (PXRD) for presence of a new phase. Mechanochemistry is not only a green method of screening for new phases but can also allow for faster analysis of the coformers or conditions that afford a new phase, when compared to crystal growth from solution.[16–18]

Resveratrol (3,4′,5-trihydroxy-*trans*-stilbene, RSV, Scheme 1) is a naturally occurring polyphenol found in many different foods, including peanuts and grapes. It is a known antioxidant, bears three hydroxyl groups, and has many other benefits including anti-inflammatory, cardioprotective, and neuroprotective properties.[19–23] However, it is poorly soluble in water, which limits its use as a medication or supplement. 4-Aminopyridine (4AP, Scheme 1) is a small-molecule drug approved by the U.S. FDA for the treatment of multiple sclerosis (MS). 4AP has been shown to improve walking function in patients with the disease and is generally well tolerated.[24] The most significant side effect of 4AP is seizures, which may occur if drug concentration builds up in the blood plasma. One common way this happens is through kidney damage, which prevents proper excretion of 4AP from the blood.[24,25]

RSV is known to help restore the integrity of the blood–brain barrier, which may help mitigate progression of MS.[26–28] Furthermore, RSV, like other antioxidants, could help prevent kidney damage, avoiding buildup of 4AP in the blood.[29] Therefore, we explored cocrystallization as a method to prepare new solid materials of these two biologically-active compounds. We expected intermolecular hydrogen-bond formation to be the primary driver for self-assembly.

During cocrystallization and form screening, we discovered two phases that exhibit different stoichiometries, water inclusion, and site of proton transfer. Based on literature precedent, the first deprotonation of RSV is expected at the 4′-phenol (see Scheme 1). Here, we demonstrate two unique crystalline phases of RSV wherein deprotonation occurs at different phenol sites (4′ and 3). Furthermore, we developed a method to reversibly interconvert between the two obtained phases using mechanochemistry. Reversible interconversion of multicomponent pharmaceutical solids has been observed in a few cases; however, interconversion between phases with differing stoichiometry, water inclusion, and deprotonation site are rare. Both phases also exhibit a remarkable increase in aqueous solubility when compared to RSV, and electrostatic potential, intermolecular interaction potential, and lattice energy calculations offer insight into the structural stability of the two phases. The deprotonation of RSV is known to impact its antioxidant activity,[30] and this work describes the first two solid forms of RSV in an ionic (deprotonated) state, which is relevant to antioxidants/nutraceuticals marketed in the solid phase.

## 2. Experimental

### 2.1. Materials

Resveratrol (RSV) was purchased from Oakwood Chemical (Columbia, SC, USA). 4-Aminopyridine (4AP) was purchased from Acros Organics (Fair Lawn, NJ, USA). Ethyl acetate and hexanes were purchased from Fisher Scientific (Fair Lawn, NJ, USA). All chemicals were used as received.

### 2.2. Initial preparation of new phases

The 1 : 1 ionic cocrystal phase (RSV·4AP, phase **1**) was initially produced *via* a slurry method by adding RSV and 4AP in a 1 : 1 molar ratio to a small amount of ethyl acetate or chloroform and stirring overnight. The solvent was subsequently evaporated, and the solid was analyzed *via* PXRD. Nearly quantitative formation of phase **1** was observed in all slurry experiments.

The 1 : 2 hydrate phase (RSV·2(4AP)·$H_2O$, phase **2**) was initially produced *via* a slurry method by adding RSV and 4AP in a 1 : 3 molar ratio to a small amount of chloroform and stirring overnight. The solvent was subsequently evaporated, and the solid was analyzed *via* PXRD. Near quantitative formation of phase **2** was observed in all slurry experiments.

### 2.3. Liquid-assisted grinding (LAG) experiments

LAG experiments were performed using a FlackTek SpeedMixer 300-100 SE purchased from FlackTek manufacturing. Stainless steel milling jars and milling balls were acquired from Form-Tech Scientific. Prior to milling, the jars were placed in a custom holder acquired from FlackTek. Milling was performed in five-minute increments followed by a 30 second rest period before continuing.

Phase **1** was prepared by placing equimolar amounts of RSV (70.8 mg, 0.31 mmol) and 4AP (29.2 mg, 0.31 mmol) along with 30 μL ethyl acetate and one 10 mm stainless steel grinding ball in a 15 mL stainless steel milling jar. The mixture was then milled at 1500 rpm for 10 minutes. The product was allowed to air dry for a few hours, then PXRD was performed.

Phase **2** was prepared by placing 44.8 mg RSV (0.2 mmol), 55.3 mg 4AP (0.6 mmol), 30 μL $H_2O$, and one 10 mm stainless steel grinding ball in a 15 mL stainless steel milling jar. The

mixture was then milled at 1500 rpm for 10 minutes. The product was allowed to air dry for a few hours, then PXRD was performed. Phase **2** was also prepared by milling RSV and 4AP in a 1 : 2.5 or 1 : 2 molar ratio with the same procedure.

### 2.4. Interconversion experiments using LAG

Interconversion experiments were performed in 15 mL stainless steel milling jars with one 10 mm stainless steel grinding ball. First, phase **1** was produced by placing 70.8 mg (0.31 mmol) RSV, 29.2 mg (0.31 mmol) 4AP, and 30 μL ethyl acetate in a milling jar, which was then milled at 1500 rpm for 10 minutes. PXRD confirmed formation of phase **1**. To convert phase **1** into phase **2**, 100 mg of phase **1** was placed in a milling jar, followed by addition of 58.4 mg (0.62 mmol) 4AP and 30 μL $H_2O$. The components were then milled at 1500 rpm for 10 minutes, which afforded phase **2** as evidenced by PXRD. To convert phase **2** into phase **1**, 100 mg of phase **2** was placed in a milling jar, followed by 89.4 mg (0.39 mmol) RSV and 30 μL ethyl acetate. The components were then milled at 1500 rpm for 10 minutes, which yielded phase **1** as evidenced by PXRD.

These conversions were able to be repeated twice, in sequence, to afford the appropriate phases, *i.e.*, phase **1** was produced, then converted into phase **2**, then converted back into phase **1**, then converted into phase **2** a second time, then converted back into phase **1**.

### 2.5. Role of stoichiometry and solvent on interconversion in LAG experiments

To determine if stoichiometry was the primary condition for conversion, 100 mg of phase **1** was placed in a milling jar, followed by addition of 58.4 mg 4AP. The components were then milled at 1500 rpm for 10 minutes and analyzed *via* PXRD. Similarly, 100 mg of phase **2** was placed in a milling jar, followed by addition of 89.4 mg RSV. The components were then milled at 1500 rpm for 10 minutes and analyzed *via* PXRD.

To determine if solvent was the primary condition for conversion, 100 mg of phase **1** was placed in a milling jar, followed by 30 μL $H_2O$. The components were then milled at 1500 rpm for 10 minutes and analyzed *via* PXRD. Similarly, 100 mg of phase **2** was placed in a milling jar, followed by addition of 30 μL ethyl acetate. The components were then milled at 1500 rpm for 10 minutes and analyzed *via* PXRD.

### 2.6. Preparation of single crystals

When crystallizing either phase, methanol, ethanol, and water were avoided because deprotonated RSV reacts with these solvents, degrading in solution.

Crystals of phase **1** were grown by dissolving 60.5 mg RSV (0.27 mmol) and 25.0 mg 4AP (0.27 mmol) in 3 mL ethyl acetate. Slow evaporation of the solution yielded crystals suitable for X-ray diffraction.

Crystals of phase **1** were also grown by using the products obtained from interconversion experiments with a 1 : 1 molar ratio. Approximately 10 mg of the product was dissolved in 2 mL ethyl acetate in a small vial. The small vial was then placed inside a larger vial and surrounded by hexanes. After several days of allowing the vapors to diffuse, crystals suitable for X-ray diffraction grew on the inside wall of the small vial.

Crystals of phase **2** were grown by dissolving approximately 5 mg of the product from LAG (1 : 3 ratio RSV : 4AP) in 3 mL ethyl acetate in a small vial. The small vial was placed inside a larger vial and surrounded by hexanes. After several days of allowing the vapors to diffuse, crystals suitable for X-ray diffraction grew on the inside wall of the small vial. Crystals of phase **2** were also grown by dissolving 10.5 mg of the product from LAG (1 : 2.5 ratio RSV : 4AP) in 2 mL ethyl acetate in a small vial, then vapor diffusing against hexanes. After several days of vapor diffusion, crystals suitable for X-ray diffraction grew on the inside wall of the vial.

### 2.7. Stability testing

The stability of phase **1** and phase **2** were each assessed in three different environments (I–III, below) under ambient or accelerated conditions. Ambient temperature and humidity were measured as 20 °C and 30%, respectively.

(I) A small portion of solid was placed in a vial open to ambient temperature and humidity and allowed to sit for one week.

(II) A small portion of solid was placed in a vial open to ambient atmosphere and was heated at 50 °C under ambient humidity for one week.

(III) A small portion of solid was placed in a small vial, which was placed inside a larger vial filled with water. The larger vial was heated to 50 °C, then capped. The solids were allowed to sit for one week at elevated temperature and humidity.

After one week, each sample was analyzed *via* PXRD to determine relative stability under each condition.

### 2.8. Single-crystal X-ray diffraction (SCXRD)

X-ray data was collected using a Rigaku XtaLAB Synergy-i Kappa diffractometer equipped with a PhotonJet-i X-ray source operated at 50 W (50 kV, 1 mA) to generate Cu Kα radiation ($\lambda$ = 1.54178 Å) and a HyPix-6000HE HPC detector. Full details are included in Section S2, SI.

### 2.9. Powder X-ray diffraction (PXRD)

PXRD patterns were collected using a Rigaku Miniflex 6G benchtop powder diffractometer in Bragg–Brentano geometry. An X-ray diffraction pattern was obtained by scanning a $2\theta$ range of 3–60°, step size = 0.02°, and scan time of 5° $min^{-1}$. The X-ray source was Cu Kα radiation ($\lambda$ = 1.5418 Å) with an anode voltage of 40 kV and a current of 15 mA. Diffraction intensities were recorded on a position sensitive detector (D/teX Ultra).

### 2.10. Fourier transform infrared (FTIR) spectroscopy

FTIR data were collected using an Agilent Carey 630 FTIR Spectrometer equipped with an ATR sampling module.

### 2.11. Nuclear magnetic resonance (NMR) spectroscopy

$^1$H NMR data were collected using a Bruker AVII+ 300 MHz spectrometer. Single crystals were dissolved in DMSO-$d_6$ for data collection.

### 2.12. Differential scanning calorimetry (DSC)

DSC data was collected using a TA Instruments DSC250. A RCS 90 refrigerated cooling system was equipped, using a nitrogen atmosphere (50 mL $min^{-1}$). Samples were run in aluminum pans with hermetic lids, at a heating rate of 10 °C $min^{-1}$.

### 2.13. Thermogravimetric analysis (TGA)

TGA data was collected using a TA Instruments TGA Q50. Samples were run in a platinum pan, with a heating rate of 10 °C $min^{-1}$. A nitrogen atmosphere was used with gas flow set at 40 mL $min^{-1}$.

### 2.14. Solubility testing

Solubility studies were conducted in pH 1.2 buffer *via* the shake-flask method.[31] Excess solid of either phase was suspended in 2 mL of buffer and stirred at 25 °C for one day. The solution was then allowed to sit for one hour before filtering through a Fisherbrand 13 mm PTFE, non-sterile, 0.2 μm pore size syringe filter. The filtrate was diluted and analyzed *via* UV-vis spectroscopy.

### 2.15. UV-vis spectroscopy

UV-vis data was collected on an Agilent 8453 UV-vis spectrophotometer.

### 2.16. Calculations

The p$K_a$ values were calculated using the plugins for structure property prediction and calculation, Playground 1.6.2, from ChemAxon.[32] The electrostatic potential maps were generated in Spartan'24, version 1.3.1.[33] Calculations were performed using DFT method, using the B3LYP basis set and 6-311++G** level of theory. Calculations were conducted with geometry-optimized molecules as well as molecules modeled in their crystalline geometry without additional geometry optimization. Lattice energies and intermolecular potentials were calculated using DREIDING II forcefield,[34–36] with Evjen electrostatic correction[37] and a limiting radius of 30 Å, using the VisualHabit[38] implementation in Mercury v. 2025.3.3.[39]

## 3. Results and discussion

### 3.1. Preparation of pharmaceutical solids and structural features

Electrostatic potential calculations for 4AP and RSV were performed using geometry-optimized molecules to assess cocrystallization likelihood. For 4AP, the geometry-optimized structure shows that the amine groups exhibit the highest potential (221 and 212 kJ $mol^{-1}$), while the pyridyl nitrogen corresponds to the minima on the surface (−211 kJ $mol^{-1}$, Fig. 1a). For RSV, the geometry-optimized structure shows that the 4′-phenol exhibits the highest potential (270 kJ $mol^{-1}$), while the 3- and 5-phenol groups minimize to the *syn–anti* geometry and exhibit lower and equal potentials (254 kJ $mol^{-1}$, Fig. 1b). The oxygen atoms of RSV correspond to the minima on the surface (ranging from −124 to −135 kJ $mol^{-1}$). Notably, the

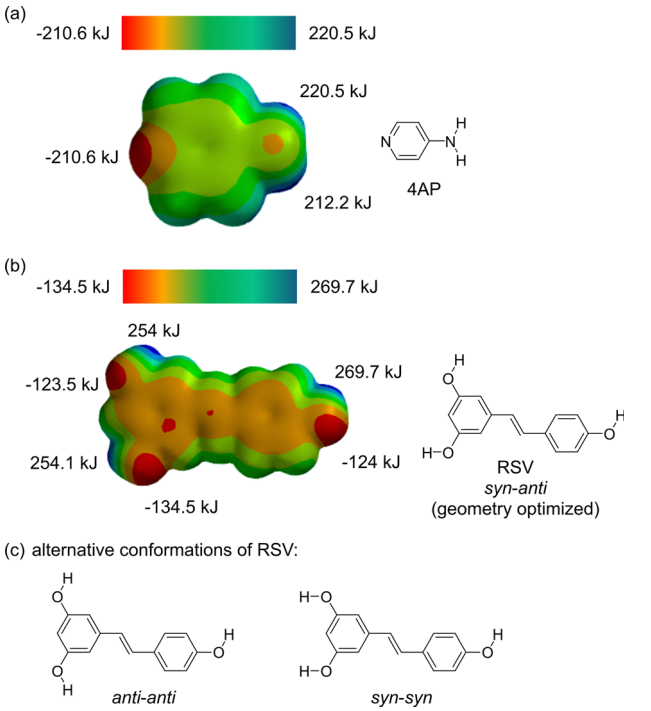


Fig. 1 Electrostatic potential maps of (a) 4AP and (b) RSV with corresponding skeletal structures of the geometry-optimized structure. (c) Additional conformations RSV can adopt.

pyridine of 4AP exhibits a more negative potential than the oxygen atoms of RSV, and all three phenols of RSV exhibit a more positive potential than the amine groups of 4AP, indicating cocrystallization between the two species *via* hydrogen bonding is favorable.

A molecular cocrystal typically contains at least two components in a stoichiometric ratio and the components are neutral. On the other hand, an ionic cocrystal contains at least three components: a cation, an anion, and a neutral molecule or ionic coformer.[40,41] A 1 : 1 ionic cocrystal of RSV·4AP (phase **1**) was initially produced using a slurry method in ethyl acetate, and LAG using ethyl acetate afforded the same phase (Fig. S1 and S2). Dissolution of the powder obtained from the slurry in ethyl acetate followed by slow evaporation yielded crystals suitable for characterization *via* SCXRD (Table S1). Phase **1** is an ionic cocrystal and the components crystallized in the space group $P\bar{1}$. The asymmetric unit includes four unique components, a neutral RSV molecule, a $RSV^-$ anion, and two 4AP molecules that share the remaining proton part of the time (see crystallographic modeling details in SI). PXRD demonstrated bulk phase purity (Fig. S3), FTIR spectroscopy supported formation of a new phase (Fig. S10), and $^1$H NMR spectroscopy confirmed a 1 : 1 ratio of the components (Fig. S11). The FTIR spectrum of phase **1** included signals for the key functional groups in both molecular components (*i.e.*, N–H, C=N, C–O, and multiple aromatic stretches), all of which are shifted in **1** compared to the individual components (Table S2).

In phase **1**, the $RSV^-$ anion transfers a proton from the 4′-phenol to the pyridyl nitrogen of 4AP, in agreement with the

 

electrostatic potential predictions. The two unique RSV components exhibit distinct conformations. In the neutral RSV molecule, the two rings lie nearly coplanar (twisted by 11°), and the benzenediol exhibits the *syn–anti* conformation, analogous to the geometry-optimized structure (Fig. 1b). On the other hand, the rings of the $RSV^-$ anion are twisted from coplanarity by 37°, and the benzenediol exhibits the *anti–anti* conformation (Fig. 1c). One key component of the self-assembled solid is the formation of four-component hydrogen-bonded rings. The rings include one 4AP molecule, two $RSV^-$ anions, and one neutral RSV molecule (Fig. 2). The rings are connected along the *c* axis *via* the neutral RSV molecule, which donates one hydrogen bond to the four-membered ring from its *anti*, 3-phenol group and donates one hydrogen bond from its 4′-phenol group to an $RSV^-$ anion (4′-position) in an adjacent ring (Fig. S13). Similar phenol···phenolate hydrogen bonds have been observed in solids containing phenols and other nutraceuticals.[42,43] The rings are also connected along the *ac* plane *via* a pair of two crystallographically unique 4AP molecules that engage in a single hydrogen bond between the protonated and neutral pyridine. Overall, the crystalline solid contains hydrogen bonds along all three dimensions.

Given the three hydrogen-bond-donor sites of RSV, we performed several additional slurry experiments to screen for other possible material phases. A new phase was identified from a slurry in chloroform using a 1 : 3 ratio of RSV : 4AP (Fig. S1). However, we were unable to obtain single crystals from the slurry material using a variety of techniques. Thus, we instead turned to LAG and milled a 1 : 3 molar ratio of RSV : 4AP in the presence of water, which afforded the new phase (Fig. S2). Vapor diffusion of this LAG product produced crystals suitable for SCXRD. This phase is a 1 : 2 monohydrate phase of RSV·2(4AP)·$H_2O$ (phase **2**, Table S1).

In initial screening experiments, grinding a 1 : 3 ratio of RSV : 4AP in the presence of water produced phase **2**, but PXRD also showed presence of excess 4AP (Fig. S2). LAG was subsequently attempted using 1 : 2 and 1 : 2.5 molar ratios (RSV : 4AP) in the presence of water to produce phase **2**. Milling in both 1 : 2 and 1 : 2.5 molar ratios afforded phase **2**, and PXRD showed a decreased presence of peaks corresponding to 4AP alone (Fig. S2). Solution-based crystallization of phase **2** was achieved using the 1 : 2.5 milling product but was not successful using the 1 : 2 milling product, indicating a slight excess of 4AP is needed for phase **2** to crystallize well from solution.

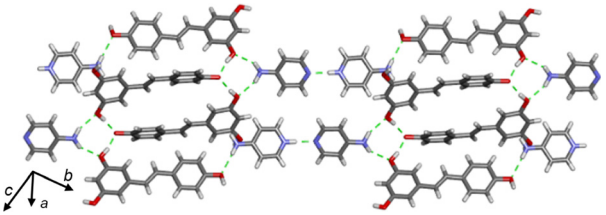


Fig. 2 X-ray crystal structure of phase **1** highlighting extensive hydrogen bonding between components. The disorder has been omitted for clarity.

The components of phase **2** crystallized in the Sohncke space group $P2_1$ as an ionic cocrystal hydrate. The asymmetric unit is comprised of one $RSV^-$ anion, one $4AP^+$ cation, one neutral 4AP molecule, and one water molecule. PXRD demonstrated phase purity of the bulk material (Fig. S3), FTIR spectroscopy indicated formation of a new phase (Fig. S10), and $^1H$ NMR spectroscopy confirmed the 1 : 2 ratio of RSV and 4AP (Fig. S12). The FTIR spectrum of phase **2** included signals for functional groups in both molecular components, analogous to phase **1** (*i.e.*, N–H, C=N, C–O, and multiple aromatic stretches), which are all shifted in the ionic cocrystal hydrate (Table S2).

In phase **2**, the $RSV^-$ anion is deprotonated at the 3-position, and the rings are twisted from coplanarity by 19°. Notably, the 3-phenol exhibits a lower potential on the electrostatic potential map when compared to the 4′-phenol (Fig. 1b). The $4AP^+$ cation is protonated at the pyridyl nitrogen. The included water molecule is a key component for the extended hydrogen-bonded assembly within phase **2**. The water molecule serves as a donor for two hydrogen bonds, one to the phenolate at the 3-position of one $RSV^-$ anion and a second to the 5-phenol of an adjacent $RSV^-$ anion. The deprotonated 3-position of the $RSV^-$ anion accepts two additional hydrogen bonds from the 5- and 4′-phenol groups of two $RSV^-$ anions to afford a sheet that extends in the *bc* plane (Fig. 3a). The water molecule also serves as the acceptor for two hydrogen bonds from the amine groups of a $4AP^+$ cation and a neutral 4AP molecule. Similar to phase **1**, the two unique 4AP components engage in a single hydrogen bond between the protonated and neutral pyridine groups, connecting the water molecules into a hydrogen-bonded chain, which extends along the *c* axis (Fig. 3b). The 4AP chains are connected to the RSV sheet along the *a* axis *via* the water molecule, as well as a hydrogen bond between the amine of a $4AP^+$ cation and 4′-phenol of an $RSV^-$ anion

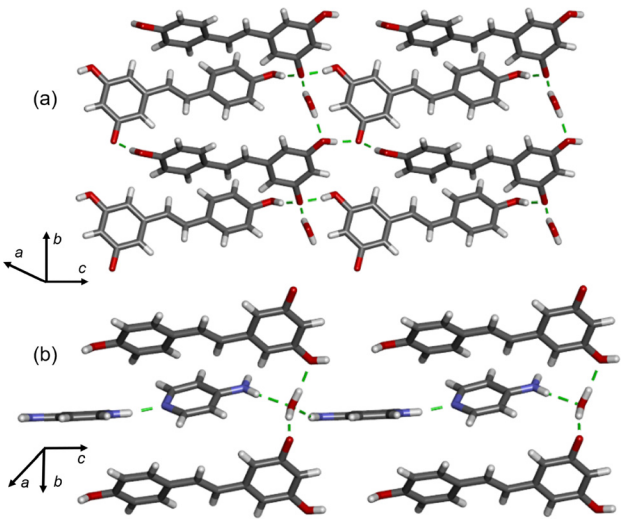


Fig. 3 X-ray crystal structure of phase **2** showing (a) hydrogen bonding involving $RSV^-$ anions with water and (b) extensive hydrogen bonding initiating at the water molecule.

(Fig. S14). Phase **2** also includes hydrogen bonds in all three dimensions.

### 3.2. Effect of RSV protonation state on antioxidant behavior

In phase **1**, RSV is deprotonated at the 4′-position, while in phase **2**, deprotonation occurs at the 3-position. Several studies have reported the bond dissociation enthalpies of RSV and concluded the 4′-hydroxyl group has the lowest bond dissociation enthalpy, proton dissociation enthalpy, and proton affinity, indicating that it will be the first site to undergo deprotonation in solution.[44] The electrostatic potential calculations above also agree that the 4′-phenol has the highest potential.

The p$K_a$ values for RSV have been measured experimentally and calculated using theory. In one case, the aqueous p$K_a$ values for RSV were measured as: p$K_{a1}$ = 8.8, p$K_{a2}$ = 9.8, and p$K_{a3}$ = 11.4,[45] while another study reported similar values of: p$K_{a1}$ = 9.16, p$K_{a2}$ = 9.77, and p$K_{a3}$ = 10.55.[46] In both cases, p$K_{a1}$ corresponds to the 4′-hydroxyl group, while p$K_{a2}$ and p$K_{a3}$ correspond to the 3- and 5-hydroxyl groups (*i.e.*, benzenediol side, Scheme 1). Using either set of values above, the p$K_a$ difference ($\Delta$p$K_a$) between protonated 4AP (p$K_a$ = 8.95)[32] and RSV is approximately 0 ($\Delta$p$K_a$ = 0.15 or −0.21), which favors a neutral cocrystal.[47,48] Using Cruz-Cabeza's equation,[48] the probability of salt formation between this molecular pair is 25–30%. A search of the Cambridge Structural Database for multicomponent solids including RSV revealed all published solids (where SCXRD is deposited) include RSV in its neutral state.[49] Phase **1** and phase **2** represent the first ionic crystalline forms of RSV.

The measured and calculated p$K_a$ values for RSV all agree that the 4′-hydroxyl group is most acidic, with one notable exception. As previously reported[50] and verified here, the p$K_a$ calculator within MarvinSketch predicts the p$K_a$ of the 3-hydroxy position of RSV to be most acidic (p$K_{a1}$ = 8.49) and the 4′-hydroxy slightly less acidic (p$K_{a2}$ = 9.13).[32] The site of deprotonation observed within phase **1** agrees with most literature; however, phase **2** is deprotonated at the 3-position, in agreement with the previous report and p$K_a$ calculator. In phase **2**, the presence of water and crystal packing forces in the structure likely supports the formation of this less stable anion in the crystalline phase.[51–53]

As related to p$K_a$ values, the antioxidant activity of RSV continues to be a highly investigated topic, and in solution, the activity is known to depend on pH. For example, Konopko and Litwinienko showed that at pH 6, RSV exhibited a significantly longer induction time (*i.e.*, suppression of lipid oxidation rate) in micelles and liposomes. This was attributed to the formation of both a 4′-radical and 4′-radical-3-anion of RSV, which, through radical rearrangement, enabled formation of RSV dimers with recovered radical-trapping functionality in solution.[30] Interestingly, Zupančič *et al.* demonstrated the antioxidant behavior of RSV was hindered at higher pH due to rapid (within minutes) degradation at pH > 9. RSV degradation at alkaline pH is associated with deprotonation, where the phenolate makes RSV more susceptible to oxidation, resulting in formation of a phenoxy radical.[54] The increase in degradation rate between pH 9 and 10 may occur because at pH 9, primarily only one phenol of RSV will be deprotonated, whereas at pH 10, two phenols will be deprotonated.

### 3.3. Thermal characterization of the pharmaceutical solids

To investigate the thermal stability of both phases, differential scanning calorimetry (DSC) and thermogravimetric analysis (TGA) were conducted. In the DSC thermogram, phase **1** shows one endothermic peak at 178 °C, corresponding to the melting point (Fig. S15). Phase **2** exhibits two endothermic signals in the DSC thermogram, corresponding to loss of water at 93 °C and melting at 169 °C (Fig. S15). The melting point of both phase **1** and phase **2** lie above the melting point of 4AP (159 °C)[55] but below the melting point of RSV (267 °C).[56]

TGA demonstrated that phase **1** and phase **2** exhibit similar broad, stepwise mass loss profiles. Phase **1** exhibits onset points at *ca.* 153 °C and *ca.* 245 °C (Fig. S16). Phase **2** exhibits loss of water at *ca.* 89 °C, and onsets at *ca.* 153 °C and *ca.* 235 °C. The first onset point in both phases occurs at a slightly higher temperature than the decomposition onset of 4AP (Fig. S16 and Table S3). Overall, the thermal properties of the two phases are quite similar, except for the loss of water, which occurs only in the hydrated ionic cocrystal.

Some cocrystal and salt hydrates have been shown to convert to their anhydrous counterparts through heating. The structures of phase **1** and phase **2** are significantly different and removal of water from **2** would require significant structural reorganization to yield **1**. Heating phase **2** at 100 °C under either ambient or inert atmosphere to drive off water afforded degradation, rather than conversion into phase **1**.

### 3.4. Stability of drug phases under ambient and accelerated conditions

The relative stability of both phases and the individual components was assessed under ambient and accelerated (50 °C/ambient humidity or 50 °C/100% humidity) conditions over a period of one week (Fig. S6–S9). After one week at ambient conditions, phase **1** exhibits partial conversion into the physical mixture, as evidenced by the peak at 24.3° in the PXRD pattern (Fig. S6). At elevated temperature, phase **1** exhibits peak broadening in the PXRD pattern, indicating a slight loss of crystallinity, though the material is largely unaffected. However, at elevated temperature and humidity, phase **1** turned slightly brown, indicative of RSV degradation. The PXRD pattern also confirms degradation, evidenced by a loss in peak intensity and slight broadening (Fig. S6). However, over all conditions, phase **1** remains the major crystalline species. These results illustrate that phase **1** is largely stable, except under hot and humid conditions, where water vapor likely reacts with the phenolate of $RSV^-$, leading to partial degradation. Phase **2** exhibits similar trends, with partial amorphization occurring under room temperature and humidity over a one-week period. At elevated temperature and ambient humidity, however, conversion of phase **2** into phase **1** is observed. The gentler heating drives water out of the crystal

 

while allowing the structure to rearrange, rather than degrade as observed during the more intense heating at 100 °C. The product was also brown after heating, indicating partial degradation of the phase as water leaves the crystal structure. In addition, heating under high humidity led to significant browning (degradation) of the product, associated with the phenolate of $RSV^-$ reacting with water vapor from the humid atmosphere. This degradation is corroborated with peak broadening and loss of intensity in the PXRD pattern, though phase integrity is maintained (Fig. S7).

The difference in discoloration (browning) between phase **1** and phase **2** at elevated temperature and high humidity is likely due to presence of water in the crystal structure of phase **2**. The included water can likely react with the phenolate of $RSV^-$ more readily than atmospheric water. These results indicate phase **1** is the more stable solid phase.

As individual solids, both molecular components demonstrate minimal degradation. 4AP exhibited minimal degradation *via* loss of peak intensity after one week at elevated temperature, and RSV only showed decreased peak intensity after heating at elevated humidity (Fig. S8 and S9). RSV exhibited browning under elevated temperature conditions, similar to its behavior in the ionic cocrystals. The components by themselves are reasonably stable due to the absence of proton transfer in these solids.

### 3.5. Solubility of drug phases

RSV exhibits incredibly low aqueous solubility (0.06 mg $mL^{-1}$) over the pH range of 1.2–6.8,[57] contributing to its limited use as a supplement or medication. The aqueous solubility of 4AP, however, is quite high ($>50$ mg $mL^{-1}$),[58] motivating its use in cocrystallization with RSV.

The shake-flask method was used to determine the aqueous solubility of phase **1** and phase **2** at pH 1.2.[31] This pH was chosen because of the limitations with RSV stability,[54] and this environment is similar to the fasting state of the stomach. At pH 1.2, both ionic cocrystal phases showed a dramatic increase in solubility when compared to RSV (Table S4). Specifically, phase **1** exhibited a solubility of $3.7 \pm 0.05$ mg $mL^{-1}$, corresponding to a 60-fold enhancement when compared to RSV. Phase **2** exhibited a solubility of $6.7 \pm 0.95$ mg $mL^{-1}$, corresponding to over a 100-fold enhancement when compared to RSV. While the solubility of both ionic cocrystal phases is significantly lower than that of 4AP, the increase in RSV solubility is unprecedented, with other cocrystals exhibiting only minimal increases in solubility, up to approximately 5× higher.[59–65] The two ionic cocrystal phases reported here are the only two examples of RSV cocrystals reaching solubility values in the mg $mL^{-1}$ range.

### 3.6. Structural influence on the properties of the drug phases

Both ionic cocrystals are sustained by numerous neutral and charge-assisted hydrogen bonds. The hydrogen bond lengths in the solids are similar and range from 2.49–3.05 Å in phase **1** and 2.52–3.01 Å in phase **2** (distances are between heavy atoms), with the ionic interactions generally being shorter. The hydrogen-bond angles lie in the range of 149°–178°. To further investigate the formation of the phenolate at different sites of RSV, the presence or absence of water in the structure, and physiochemical properties of the two phases, the lattice energies, intermolecular potentials, and additional electrostatic potentials were calculated.

The electrostatic potential maps of the geometry-optimized structures of 4AP and RSV supported cocrystallization and hydrogen-bond formation at the phenol and pyridine groups, as well as proton transfer occurrence at these sites. Alternatively, when the electrostatic potentials were calculated with the molecules in their crystalline-state geometries, the impact of the anionic/cationic nature was observed. For the $4AP^+$ cation, the pyridinium becomes the site of highest potential when the cations from both phase **1** and phase **2** are used, and the potential on the amine groups increases significantly due to the electron deficiency, which is clearly delocalized through the ring (Fig. S18). In phase **1**, two unique RSV molecules are present, one neutral and one anion. The neutral RSV exhibits similar potential values to the geometry-optimized RSV. However, the *anti*, 3-hydroxy group exhibits the highest potential, rather than the 4′-hydroxy. For the $RSV^-$ anions within phase **1** and phase **2**, the phenolate groups become the minima on the surfaces due to the anion. Moreover, when compared to the fully protonated RSV, the potential of the remaining two phenol groups on the $RSV^-$ anions decrease significantly and the previously electron-rich aromatic system becomes localized near the phenolate (Fig. S19). Upon formation of the phenolate, the remaining phenols of each RSV become weaker hydrogen-bond donor sites at the hydrogen, but stronger hydrogen-bond acceptors at the oxygen. Once the pyridinium is formed, the amine groups of 4AP become stronger hydrogen-bond donor sites. In phase **1**, the amines form hydrogen bonds with the phenol oxygens (strong acceptors) and in phase **2** the amines form hydrogen bonds with water and a phenol oxygen.

Examination of the intermolecular forces through intermolecular potential calculations in Mercury demonstrate the significance of electrostatics and hydrogen bonds in stabilizing both structures. The total interaction energy includes components of electrostatic, van der Waals, and hydrogen bond energies. For both phases, the hydrogen bonds between $4AP^+$ cations are one of the two most energetically significant interactions in the electrostatic and hydrogen bond components.

For phase **1**, the other most significant contributions to the hydrogen bond energies include the hydrogen bond dimers between two $RSV^-$ anions (*anti*, 3-phenol group to 4′-phenolate) and O–H···O bonds between neutral phenol groups or neutral phenol to phenolate groups (Fig. S20 and Table S5). The hydrogen bonds involving the amine groups as donors contribute less significantly, and the smallest overall contributor is the interaction between the *anti*, 3-phenol group on a neutral RSV to the 4′-phenolate of the $RSV^-$ anion.

Within phase **2**, the hydrogen bonds involving the water molecule represent four of the five most stabilizing hydrogen

bond energies in the structure (Fig. S21 and Table S6). The substantial hydrogen bonding involving water likely contributes to the formation of the less stable 3-phenolate anion of RSV. The hydrogen bonds involving the amine groups as donors contribute less significantly. The structure includes only one $RSV^-$ anion, and the O–H···O hydrogen bonds between neutral phenol and phenolate moieties are electrostatically destabilizing and offer smaller hydrogen bond contribution. Notably, the smallest overall contributor to the hydrogen bond energy is the interaction between the *syn*, 5-phenol group and the 3-phenolate. The electrostatic potential (using the crystalline-state geometry) of the 5-phenol site decreases significantly upon formation of the adjacent phenolate, supporting the lack of structural stabilization that occurs with bonding at this position.

The overall lattice energies of the two phases were also calculated using Mercury. Phase **1** exhibits more stabilizing electrostatic, van der Waals, and hydrogen bond interactions compared to phase **2**, resulting in phase **1** exhibiting a larger lattice energy ($-207$ kJ mol$^{-1}$) relative to phase **2** ($-168$ kJ mol$^{-1}$). Differences in the electrostatic and van der Waals contributions play the most significant role in the energetic differences (Table S7). The lower lattice energy of phase **2** is supported by the higher solubility and lower melting point values relative to phase **1**.

### 3.7. Mechanochemical interconversion between drug phases

During attempts to grow single crystals of phase **2** using the product obtained from 1 : 3 milling experiments, several samples afforded crystals of phase **1** with excess 4AP. Given this result, we explored the idea that interconversion between these two phases may be possible and chose to use mechanochemistry for the experiments. Due to differences in stoichiometry and water inclusion between phase **1** and **2**, the stoichiometry of the components and solvent used in LAG were investigated as factors that could influence the milling product.

Initially, phase **1** was formed *via* LAG as described above. 4AP was then added to the product to raise the stoichiometry to 1 : 3, and the mixture was milled again with 30 μL water, which afforded the hydrate, phase **2**. To convert phase **2** back into phase **1**, RSV and 30 μL ethyl acetate were added to the product to adjust the ratio to 1 : 1 RSV : 4AP, and the material was subjected to milling, which yielded phase **1**. This process was repeated once more in succession, and each product was characterized using *ex situ* PXRD. We successfully achieved two full interconversion cycles, *i.e.* **1** to **2** to **1** to **2** to **1** (Fig. 4). Each product obtained from the interconversion milling experiments was also able to be crystallized in solution *via* vapor diffusion.

### 3.8. Factors that influence polymorph conversion or interconversion

In single-component solids, several examples of converting one polymorph into another have been reported. Specifically, pressure,[66,67] heat,[13,68] and solvent choice,[69–71] used either in solution-based crystallization or as an additive in grinding, have all been used to convert one polymorph into another. The addition of a small amount of impurity or additive can also play a role in conversion.[70,72] The same experimental conditions above can also influence polymorphism in multicomponent solids.[73–80] Conversion, and especially interconversion, in multicomponent systems is rarer than for single-component systems due to the added complexity of a second species present in the solid phase. In theory, a conversion experiment could instead afford destruction of the multicomponent phase with acquisition of the individual components, rather than conversion to a second multicomponent phase.

Mechanochemical methods have been used to achieve interconversion, and one mechanism has been attributed to grinding increasing solvent contact and enhancing surface solvation effects.[76,81] With mechanochemistry, the amount of added solvent can play a large role,[76,82] and the milling assembly materials can also enable polymorph interconversion.[83] The hardness of milling balls or jar materials affects the amount of energy input into the system, which influences phase conversion.

One condition specific to multicomponent systems is the stoichiometry of the components. In solids that exhibit differences in stoichiometry or solvent inclusion, the phase transformation can be achieved through addition of the differing reagent or solvent.[68,79,84,85] For example, Cinčić, Friščić, and coworkers showed interconversion between three halogen-bonded cocrystals with different stoichiometries.[86] Recently, Deka, Thakuria, and coworkers demonstrated a system based on *trans*-aconitic acid and nicotinamide, where one phase is a different stoichiometry than the other two, and also exists as a salt instead of a cocrystal.[87] Conversion from a 1 : 1 salt hydrate

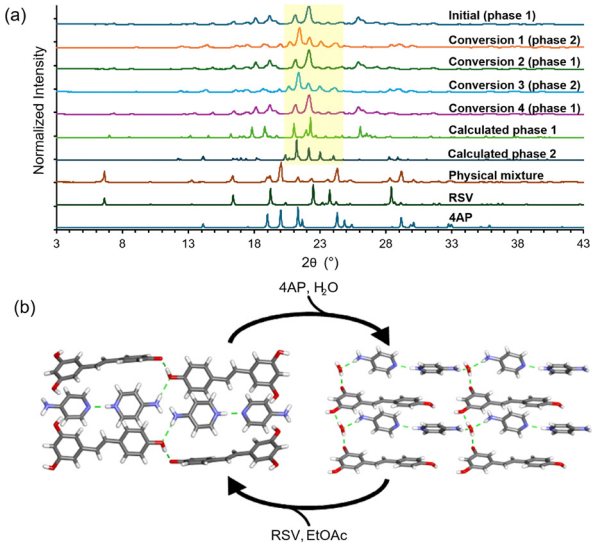


Fig. 4 (a) PXRD patterns highlighting reversible interconversion between phase **1** and phase **2** and (b) schematic of interconversion process noting reactants and solvents. The yellow transparent box highlights signals used in identifying phase **1** (two peaks) and phase **2** (four peaks of descending intensity). The calculated patterns for phase **1** and phase **2** are shifted by $-0.5°$ $2\theta$ to account for temperature difference between SCXRD and PXRD measurements.

to a 1 : 2 cocrystal hydrate required the addition of one equivalent nicotinamide and isopropanol, where conversion backwards required addition of one equivalent *trans*-aconitic acid and water.

To determine if a change in solvent and stoichiometry are both required for conversion between phases **1** and **2**, additional interconversion experiments were conducted. Only one of the two inputs was varied at a time. Neither LAG of phase **1** in the presence of water nor LAG of phase **2** in the presence of ethyl acetate enabled conversion to the other phase, and the original phase was retained (Fig. S4 and S5). Neat milling of phase **1** in the presence of additional 4AP and neat milling of phase **2** in the presence of additional RSV also afforded the original phases, with additional signals in the PXRD patterns corresponding to the added reagent (Fig. S4 and S5). Thus, interconversion between phases mechanochemically is dependent on both the stoichiometry of the components, as well as the LAG solvent.

In other systems where conversion or interconversion between two ionic forms is observed, both phases exhibit deprotonation at the same site,[79,84] with one exception. Martí-Rujas and coworkers demonstrated a system of 5-sulfosalicylic acid and 4,4′-diaminodiphenylmethane with three polymorphs.[88] In two polymorphs, deprotonation occurs at both the sulfonic acid and carboxylic acid groups, whereas the third polymorph only exhibits deprotonation at the more acidic sulfonic acid group. Notably, the deprotonation differences are between different functional groups (sulfonic *vs.* carboxylic acid). In the work described here, interconversion of phase **1** and phase **2** is achieved by addition of differing reagents and solvent. However, unlike other systems, phase **1** and phase **2** exhibit deprotonation at different sites within RSV and the functional groups (hydroxyl) are identical.

### 3.9. Outlook and future investigations

Several antioxidants are currently used as excipients in pharmaceuticals and food products as a mean to extend shelf life, especially in pharmaceuticals susceptible to oxidative degradation.[89] For pharmaceuticals with secondary or tertiary amines, nitrosamine formation is also a major concern, and antioxidants have been shown to be effective in inhibiting nitrosamine formation.[90] RSV has been previously reported to stabilize insulin[91] and may offer a superior solid form of 4AP. The presence of $RSV^{-}$ in the solid may offer increased antioxidant efficacy compared to neutral RSV or other antioxidants alone, which may help ameliorate kidney dysfunction and prevent increased blood plasma levels of 4AP. Although full efficacy studies are currently lacking, administration of RSV to mice with MS has been shown to improve clinical parameters, inflammatory markers, markers for oxidative stress, and demyelination in experimental studies.[92–97]

## 4. Conclusions

In conclusion, two ionic cocrystals of RSV and 4AP were produced, with different stoichiometries, water inclusion, and site of proton transfer. Electrostatic potential calculations support formation of hydrogen bonds between the components. Anhydrous phase **1** exhibits a higher lattice energy, higher melting point, and lower solubility, compared to hydrate phase **2**. Moreover, phase **1** was more stable than phase **2** under accelerated aging conditions. The two phases can be interconverted using mechanochemical methods *via* addition of one reagent and an appropriate solvent to the reaction mixture. All interconversion products were able to be crystallized from solution, allowing for selective production of one phase. The deprotonation of RSV in these two solid phases is novel, as is the use of mechanochemistry to control the state of deprotonation among two identical functional groups. RSV has been previously used in the stabilization of other pharmaceuticals[91] and is currently marketed as a supplement. The two phases described here may exhibit different antioxidant potential in the solid phase, given the reported difference in reactivities of the phenol sites.[44,98] Both ionic solids exhibit significant improvement in aqueous solubility compared to RSV alone, reaching the ;mg $mL^{-1}$ level. Although further testing is required, the combination of a multiple sclerosis drug with an ionic RSV could offer unique drug-antioxidant properties.

## Conflicts of interest

There are no conflicts to declare.

## Data availability

The data supporting this article have been included as part of the supplementary information (SI). Supplementary information (SI): experimental details, X-ray data, IR and NMR spectra, thermal data, and calculation results. See DOI: https://doi.org/10.1039/d5tb02000j.

CCDC 2473744 and 2473745 contain the supplementary crystallographic data for this paper.[99a,b]

## Acknowledgements

Research reported in this publication was supported by the National Institute of General Medical Sciences (NIGMS) of the National Institutes of Health (NIH) under award number R35GM160214 to K. M. H. The content is solely the responsibility of the authors and does not necessarily represent the official views of the NIH. The authors also acknowledge the University of Missouri for support.

## Notes and references

1 J. Rantanen, T. Rades and C. Strachan, *J. Pharm. Biomed. Anal.*, 2023, **236**, 115649.
2 M. Sohail Arshad, S. Zafar, B. Yousef, Y. Alyassin, R. Ali, A. AlAsiri, M.-W. Chang, Z. Ahmad, A. Ali Elkordy,

A. Faheem and K. Pitt, *Adv. Drug Delivery Rev.*, 2021, **178**, 113840.
3 N. Chieng, T. Rades and J. Aaltonen, *J. Pharm. Biomed. Anal.*, 2011, **55**, 618–644.
4 M. M. De Villiers, R. J. Terblanche, W. Liebenberg, E. Swanepoel, T. G. Dekker and M. Song, *J. Pharm. Biomed. Anal.*, 2005, **38**, 435–441.
5 T. Zhang, L. Wang, Y. Bao, Q. Yang, L. Zhou, H. Hao and C. Xie, *J. Pharm. Sci.*, 2018, **107**, 1903–1910.
6 T. Beyer, G. M. Day and S. L. Price, *J. Am. Chem. Soc.*, 2001, **123**, 5086–5094.
7 D. Chistyakov and G. Sergeev, *Pharmaceutics*, 2020, **12**, 34.
8 M. Kitamura, *Cryst. Growth Des.*, 2004, **4**, 1153–1159.
9 A. Llinàs and J. M. Goodman, *Drug Discovery Today*, 2008, **13**, 198–210.
10 S. Shen, G. Xia, Z. Jiang, Q. Shao, W. Shan and H. Wang, *Cryst. Growth Des.*, 2019, **19**, 320–327.
11 K. Linberg, P. C. Sander, F. Emmerling and A. A. L. Michalchuk, *RSC Mechanochem.*, 2024, **1**, 43–49.
12 P. Sacchi, S. E. Wright, P. Neoptolemou, G. I. Lampronti, A. K. Rajagopalan, W. Kras, C. L. Evans, P. Hodgkinson and A. J. Cruz-Cabeza, *Proc. Natl. Acad. Sci. U. S. A.*, 2024, **121**, e2319127121.
13 K. Linberg, B. Röder, D. Al-Sabbagh, F. Emmerling and A. A. L. Michalchuk, *Faraday Discuss.*, 2023, **241**, 178–193.
14 B. Rodríguez-Spong, *Adv. Drug Delivery Rev.*, 2004, **56**, 241–274.
15 S. Aitipamula, R. Banerjee, A. K. Bansal, K. Biradha, M. L. Cheney, A. R. Choudhury, G. R. Desiraju, A. G. Dikundwar, R. Dubey, N. Duggirala, P. P. Ghogale, S. Ghosh, P. K. Goswami, N. R. Goud, R. R. K. R. Jetti, P. Karpinski, P. Kaushik, D. Kumar, V. Kumar, B. Moulton, A. Mukherjee, G. Mukherjee, A. S. Myerson, V. Puri, A. Ramanan, T. Rajamannar, C. M. Reddy, N. Rodriguez-Hornedo, R. D. Rogers, T. N. G. Row, P. Sanphui, N. Shan, G. Shete, A. Singh, C. C. Sun, J. A. Swift, R. Thaimattam, T. S. Thakur, R. Kumar Thaper, S. P. Thomas, S. Tothadi, V. R. Vangala, N. Variankaval, P. Vishweshwar, D. R. Weyna and M. J. Zaworotko, *Cryst. Growth Des.*, 2012, **12**, 2147–2152.
16 T. Friščić, S. L. Childs, S. A. A. Rizvi and W. Jones, *CrystEngComm*, 2009, **11**, 418–426.
17 K. Trzeciak, M. K. Dudek and M. J. Potrzebowski, *Chem. – Eur. J.*, 2024, **30**, e202402683.
18 P. Ying, J. Yu and W. Su, *Adv. Synth. Catal.*, 2021, **363**, 1246–1271.
19 S. Stojanović, H. Sprinz and O. Brede, *Arch. Biochem. Biophys.*, 2001, **391**, 79–89.
20 D. De Sá Coutinho, M. T. Pacheco, R. L. Frozza and A. Bernardi, *Int. J. Mol. Sci.*, 2018, **19**, 1812.
21 R. Gal, L. Deres, K. Toth, R. Halmosi and T. Habon, *Int. J. Mol. Sci.*, 2021, **22**, 10152.
22 A. R. A. Ladiwala, J. C. Lin, S. S. Bale, A. M. Marcelino-Cruz, M. Bhattacharya, J. S. Dordick and P. M. Tessier, *J. Biol. Chem.*, 2010, **285**, 24228–24237.
23 M. Wiciński, A. Domanowska, E. Wódkiewicz and B. Malinowski, *Int. J. Mol. Sci.*, 2020, **21**, 2749.
24 M. Strupp, J. Teufel, A. Zwergal, R. Schniepp, K. Khodakhah and K. Feil, *Neur. Clin. Pract.*, 2017, **7**, 65–76.
25 M. T. Frejo, J. Del Pino, M. Lobo, J. García, M. A. Capo and M. J. Díaz, *Toxicol. Lett.*, 2014, **225**, 252–263.
26 C. Moussa, M. Hebron, X. Huang, J. Ahn, R. A. Rissman, P. S. Aisen and R. S. Turner, *J. Neuroinflammation*, 2017, **14**, 1.
27 Y. Kim, A. Y. Cho, H. C. Kim, D. Ryu, S. A. Jo and Y.-S. Jung, *Antioxidants*, 2022, **11**, 197.
28 D. Wang, S.-P. Li, J.-S. Fu, S. Zhang, L. Bai and L. Guo, *J. Neurophysiol.*, 2016, **116**, 2173–2179.
29 S. Chakraborty, I. Bhattacharya and R. K. Mitra, *J. Phys. Chem. B*, 2023, **127**, 8576–8585.
30 A. Konopko and G. Litwinienko, *J. Org. Chem.*, 2022, **87**, 1698–1709.
31 E. Baka, J. E. A. Comer and K. Takács-Novák, *J. Pharm. Biomed. Anal.*, 2008, **46**, 335–341.
32 *Calculator Plugins were used for structure property prediction and calculation, Playground 1.6.2*, 2024, ChemAxon, (https://www.chemaxon.com).
33 *Spartan'24 v1.3.1*, 2025, Wavefunction, Inc., Irvine, CA. https://www.wavefun.com/spartan.
34 S. L. Mayo, B. D. Olafson and W. A. Goddard, *J. Phys. Chem.*, 1990, **94**, 8897–8909.
35 D. E. Williams, *J. Chem. Phys.*, 1966, **45**, 3770–3778.
36 N. L. Allan, A. L. Rohl, D. H. Gay, C. R. A. Catlow, R. J. Davey and W. C. Mackrodt, *Faraday Discuss.*, 1993, **95**, 273–280.
37 H. M. Evjen, *Phys. Rev.*, 1932, **39**, 675–687.
38 G. Clydesdale, R. Docherty and K. J. Roberts, *Comput. Phys. Commun.*, 1991, **64**, 311–328.
39 C. F. Macrae, I. Sovago, S. J. Cottrell, P. T. A. Galek, P. McCabe, E. Pidcock, M. Platings, G. P. Shields, J. S. Stevens, M. Towler and P. A. Wood, *J. Appl. Cryst.*, 2020, **53**, 226–235.
40 D. Braga, F. Grepioni, L. Maini, S. Prosperi, R. Gobetto and M. R. Chierotti, *Chem. Commun.*, 2010, **46**, 7715.
41 T. Wang, J. S. Stevens, T. Vetter, G. F. S. Whitehead, I. J. Vitorica-Yrezabal, H. Hao and A. J. Cruz-Cabeza, *Cryst. Growth Des.*, 2018, **18**, 6973–6983.
42 S. Jin, R. Sanii, B.-Q. Song and M. J. Zaworotko, *Cryst. Growth Des.*, 2022, **22**, 4582–4591.
43 S. Jin, M. M. Haskins, Y. H. Andaloussi, R. Ouyang, J. Gong and M. J. Zaworotko, *Cryst. Growth Des.*, 2022, **22**, 6390–6397.
44 T. Phan Thi and S. Ninh The, *J. Chem.*, 2020, **2020**, 8869023.
45 J. M. López-Nicolás and F. García-Carmona, *J. Agric. Food Chem.*, 2008, **56**, 7600–7605.
46 L. Zimányi, S. Thekkan, B. Eckert, A. R. Condren, O. Dmitrenko, L. R. Kuhn, I. V. Alabugin and J. Saltiel, *J. Phys. Chem. A*, 2020, **124**, 6294–6302.
47 S. L. Childs, G. P. Stahly and A. Park, *Mol. Pharmaceutics*, 2007, **4**, 323–338.
48 A. J. Cruz-Cabeza, *CrystEngComm*, 2012, **14**, 6362.

 

49 C. R. Groom, I. J. Bruno, M. P. Lightfoot and S. C. Ward, *Acta Crystallogr., Sect. B: Struct. Sci., Cryst. Eng. Mater.*, 2016, **72**, 171–179.
50 A. R. Neves, C. Nunes, H. Amenitsch and S. Reis, *Soft Matter*, 2016, **12**, 2118–2126.
51 F. Caruso, J. Tanski, A. Villegas-Estrada and M. Rossi, *J. Agric. Food Chem.*, 2004, **52**, 7279–7285.
52 L. Yu, S. M. Reutzel-Edens and C. A. Mitchell, *Org. Process Res. Dev.*, 2000, **4**, 396–402.
53 P. Dauber and A. T. Hagler, *Acc. Chem. Res.*, 1980, **13**, 105–112.
54 Š. Zupančič, Z. Lavrič and J. Kristl, *Eur. J. Pharm. Biopharm.*, 2015, **93**, 196–204.
55 Thermodynamics Research Center, NIST Boulder Laboratories, Chris Muzny director, in *NIST Chemistry WebBook,* NIST Standard Reference Database Number 69, ed. P. J. Linstrom and W. G. Mallard, National Institute of Standards and Technology, Gaithersburg, MD, 20899, 2025.
56 R. D. C. D. Silva, J. A. Teixeira, W. D. G. Nunes, G. A. C. Zangaro, M. Pivatto, F. J. Caires and M. Ionashiro, *Food Chem.*, 2017, **237**, 561–565.
57 E.-S. Ha, D. H. Choi, I. Baek, H. Park and M.-S. Kim, *Antioxidants*, 2021, **10**, 90.
58 I. Kostadinova and N. Danchev, *Pharmacia*, 2019, **66**, 67–74.
59 Z. Zhou, W. Li, W.-J. Sun, T. Lu, H. H. Y. Tong, C. C. Sun and Y. Zheng, *Int. J. Pharm.*, 2016, **509**, 391–399.
60 D. Polati and P. Neerati, *Sci. Rep.*, 2025, **15**, 44606.
61 B. K. Mehta, S. S. Singh, S. Chaturvedi, M. Wahajuddin and T. S. Thakur, *Cryst. Growth Des.*, 2018, **18**, 1581–1592.
62 J. Wei, M. Inam, H. Mo, J. Huang, H. Zhao, A. Zhong, X. Tang, E. Deng, C. Xu, X. Chen, H. Mao, W. Chen, J. Mo and Y. Zhu, *Int. J. Pharm.: X*, 2025, **10**, 100386.
63 R.-A. Mitran, S. Ioniță, D. Lincu, E. M. Soare, I. Atkinson, A. Rusu, J. Pandele-Cușu, C. Iordache, I. Pongratz, M. M. Pop and V. Fruth, *Materials*, 2024, **17**, 3145.
64 C. Dal Magro, A. E. dos Santos, M. M. Ribas, G. P. S. Aguiar, C. R. B. Volfe, M. L. L. C. Lopes, A. M. Siebel, L. G. Müller, A. J. Bortoluzzi, M. Lanza and J. V. Oliveira, *J. Supercrit. Fluids*, 2021, **171**, 105190.
65 L. Chen, X.-Q. Ma, H.-L. Wu, S. Zhang, J.-F. Chen, N. Lin and Q. Chen, *Cryst. Growth Des.*, 2025, **25**, 9899–9907.
66 T. Okumura, M. Ishida, K. Takayama and M. Otsuka, *J. Pharm. Sci.*, 2006, **95**, 689–700.
67 A. G. Landers and T. B. Brill, *J. Phys. Chem.*, 1980, **84**, 3573–3577.
68 B. Nath and J. B. Baruah, *Cryst. Growth Des.*, 2013, **13**, 5146–5155.
69 A. V. Trask, N. Shan, W. D. S. Motherwell, W. Jones, S. Feng, R. B. H. Tan and K. J. Carpenter, *Chem. Commun.*, 2005, 880–882.
70 A. M. Belenguer, G. I. Lampronti, A. A. L. Michalchuk, F. Emmerling and J. K. M. Sanders, *CrystEngComm*, 2022, **24**, 4256–4261.
71 E. S. Ferrari, R. J. Davey, W. I. Cross, A. L. Gillon and C. S. Towler, *Cryst. Growth Des.*, 2003, **3**, 53–60.
72 S.-Y. Lin, C.-H. Hsu and W.-T. Ke, *Int. J. Pharm.*, 2010, **396**, 83–90.
73 D. Braga, S. d'Agostino and F. Grepioni, *Cryst. Growth Des.*, 2012, **12**, 4880–4889.
74 F. Fischer, G. Scholz, S. Benemann, K. Rademann and F. Emmerling, *CrystEngComm*, 2014, **16**, 8272–8278.
75 D. Hasa, E. Carlino and W. Jones, *Cryst. Growth Des.*, 2016, **16**, 1772–1779.
76 A. M. Belenguer, G. I. Lampronti, N. De Mitri, M. Driver, C. A. Hunter and J. K. M. Sanders, *J. Am. Chem. Soc.*, 2018, **140**, 17051–17059.
77 M. Morales-Santana, S. Chong-Canto, J. M. Santiago-Quintana, F. J. Martínez-Martínez, E. V. García-Báez, A. Cruz, S. Rojas-Lima and I. I. Padilla-Martínez, *CrystEngComm*, 2022, **24**, 1017–1034.
78 L. Loots, J. P. O'Connor, T. Le Roex and D. A. Haynes, *Cryst. Growth Des.*, 2015, **15**, 5849–5857.
79 W. Duan, B. Liu, N. Gong, A. Famulari and F. Guo, *Cryst. Growth Des.*, 2020, **20**, 7606–7614.
80 V. M. Abbinante, M. Zampieri, G. Barreca and N. Masciocchi, *Molecules*, 2021, **26**, 65.
81 A. M. Belenguer, G. I. Lampronti, A. J. Cruz-Cabeza, C. A. Hunter and J. K. M. Sanders, *Chem. Sci.*, 2016, **7**, 6617–6627.
82 M. Sheikhzadeh, S. Murad and S. Rohani, *J. Pharm. Biomed. Anal.*, 2007, **45**, 227–236.
83 L. S. Germann, M. Arhangelskis, M. Etter, R. E. Dinnebier and T. Friščić, *Chem. Sci.*, 2020, **11**, 10092–10100.
84 L. Loots, H. Wahl, L. Van Der Westhuizen, D. A. Haynes and T. Le Roex, *Chem. Commun.*, 2012, **48**, 11507–11509.
85 R. Kaur, B. V. Lalithalakshmi and T. N. Guru Row, *Cryst. Growth Des.*, 2014, **14**, 2614–2620.
86 M. Arhangelskis, F. Topić, P. Hindle, R. Tran, A. J. Morris, D. Cinčić and T. Friščić, *Chem. Commun.*, 2020, **56**, 8293–8296.
87 D. Gogoi, K. J. Kalita, N. Biswakarma, M. Arhangelskis, R. C. Deka and R. Thakuria, *RSC Mechanochem.*, 2024, **1**, 452–464.
88 H. Liu, Y.-F. Xie, Z. Pan, A. Famulari, F. Guo, Z. Zhou and J. Martí-Rujas, *Cryst. Growth Des.*, 2014, **14**, 6528–6536.
89 M. T. Celestino, U. D. O. Magalhães, A. G. M. Fraga, F. A. D. Carmo, V. Lione, H. C. Castro, V. P. D. Sousa, C. R. Rodrigues and L. M. Cabral, *Braz. J. Pharm. Sci.*, 2012, **48**, 405–415.
90 Y. Chiang Yu, D. Lu, B. Rege and J. E. Polli, *J. Pharm. Sci.*, 2024, **113**, 2215–2222.
91 B. K. Pathak, D. Das, S. Bhakta, P. Chakrabarti and J. Sengupta, *J. Comput.-Aided Mol. Des.*, 2020, **34**, 915–927.
92 P. H. Villar-Delfino, R. P. Santos, P. P. Christo, J. A. Nogueira-Machado and C. M. O. Volpe, *Explor. Neurosci.*, 2024, **3**, 362–374.
93 N. P. Singh, V. L. Hegde, L. J. Hofseth, M. Nagarkatti and P. Nagarkatti, *Mol. Pharmacol.*, 2007, **72**, 1508–1521.
94 T. J. Imler and T. M. Petro, *Int. Immunopharmacol.*, 2009, **9**, 134–143.

95 K. S. Shindler, E. Ventura, M. Dutt, P. Elliott, D. C. Fitzgerald and A. Rostami, *J. Neuro-Ophthalmol.*, 2010, **30**, 328–339.
96 H. R. Ghaiad, M. M. Nooh, M. M. El-Sawalhi and A. A. Shaheen, *Mol. Neurobiol.*, 2017, **54**, 3219–3229.
97 K. A. O. Gandy, J. Zhang, P. Nagarkatti and M. Nagarkatti, *J. Neuroimmune Pharmacol.*, 2019, **14**, 462–477.
98 L. A. Stivala, M. Savio, F. Carafoli, P. Perucca, L. Bianchi, G. Maga, L. Forti, U. M. Pagnoni, A. Albini, E. Prosperi and V. Vannini, *J. Biol. Chem.*, 2001, **276**, 22586–22594.
99 (*a*) CCDC 2473744: Experimental Crystal Structure Determination, 2026, DOI: 10.5517/ccdc.csd.cc2p1463; (*b*) CCDC 2473745: Experimental Crystal Structure Determination, 2026, DOI: 10.5517/ccdc.csd.cc2p1474.

 